UCRL 15800

P08362809

ANALYSIS OF BOLING'S LASER-DAMAGE MORPHOLOGY

M. Sparks

MASTER

M S Consultants Incorporated

Santa Monica, CA 90401

Final Technical Report

15 August 1980

Prepared for

Lawrence Livermore Laboratory

SECURITY CLASSIFICATION OF THIS PAGE (When Data Entered)

REPORT DOCUMENTATION PAGE	READ INSTRUCTIONS BEFORE COMPLETING FORM
1. REPORT NUMBER / 2. GOVT ACCESSION NO.	3. RECIPIENT'S CATALOG NUMBER
4. TITLE (and Subtitle) ANALYSIS OF BOLIN 'S LASER-DAMAGE MORPHOLOGY	5. TYPE OF REPORT & PERIOD COVERED FINAL - 2-12-80 through 9-15-80
	6. PERFORMING ORG. REPORT NUMBER
7. AUTHOR(s) Marshall S. Sparks	8. CONTRACT OR GRANT NUMBER(s) 8362809
9. PERFORMING ORGANIZATION NAME AND ADDRESS M. S. Consultants, Inc. 1640 Fifth Street, Suite 216 Santa Monica, CA 90401	10. PROGRAM ELEMENT, PROJECT, TASK AREA & WORK UNIT NUMBERS
11. CONTROLLING OFFICE NAME AND ADDRESS H. Pitkin 669 University of California Livermore, CA	12. REPORT DATE 9-15-80 13. NUMBER OF PAGES 56
14. MONITORING AGENCY NAME & ADDRESS(if different from Controlling Office)	15. SECURITY CLASS. (of this report) Unclassified 15a. DECLASSIFICATION/DOWNGRADING SCHEDULE
16. DISTRIBUTION STATEMENT (of this Report)	
17. DISTRIBUTION STATEMENT (of the abstract entered in Block 20, if different from Report)	
18. SUPPLEMENTARY NOTES	
19. KEY WORDS (Continue on reverse side if necessary and identify by block number) Damage, glass, isolated spot, laser, morphology, plasma, prism, scattering, theory, total-internal reflection.	

20. ABSTRACT (Continue on reverse side if necessary and identify by block number)

Beling observed that his total-internal-reflection laser-damage sites in glass closely resembled the scattering cross section for small (ka << 1), perfectly conducting sphere and suggested that a very small plasma formed and grew to a larger size, still with ka << 1 satisfied. Even with ka = 1, for which the cross section is different from that observed, the scattered field still is too small to explain the damage in terms of constructive interference between the incident- and scattered fields. Furthermore,

DD FORM 1 JAN 73 1473 EDITION OF 1 NOV 65 IS OBSOLETE

SECURITY CLASSIFICATION OF THIS PAGE (When Data Entered)

20.
the characteristic shape of the scattering cross section that matches the damage patterns is for circular polarization or unpolarized light, in contrast to the experimental plane polarizations. Extending the ideas to include effects of the scattered field outside the glass, such as plasma formation, and to include the correct field (with interesting polarization, including longitudinal circular polarization at certain distances from the surface) incident on the sphere may explain the experiments. Additional experiments and analysis would be useful to determine if the extended model is valid and to investigate related materials improvement, nondestructive testing, and the relation between laser damage, plasma initiation, and failure under stress, all initiated at small isolated spots.

TABLE OF CONTENTS

	page
Abstract	5
I. Introduction	6
II. Development of the Original Ideas	10
III. Modification of the Original Ideas	20
IV. Scattering from a Perfectly Conducting Sphere	26
V. Suggested Additional Investigations	32
VI. Acknowledgements	36
Appendix A: Near- and Far-Zone Expressions for Small Spheres	37
References	40
Figure Captions	42

ABSTRACT

Boling observed that his total-internal-reflection laser-damage sites in glass closely resembled the scattering cross section for a small ($ka \ll 1$), perfectly conducting sphere and suggested that a very small plasma formed and grew to a larger size, still with $ka \ll 1$ satisfied. Even with $ka = 1$, for which the cross section is different from that observed, the scattered field still is too small to explain the damage in terms of constructive interference between the incident- and scattered-fields. Furthermore, the characteristic shape of the scattering cross section that matches the damage patterns is for circular polarization or unpolarized light, in contrast to the experimental plane polarizations. Extending the ideas to include effects of the scattered field outside the glass, such as plasma formation, and to include the correct field (with interesting polarization, including longitudinal circular polarization at certain distances from the surface) incident on the sphere may explain the experiments. Additional experiments and analysis would be useful to determine if the extended model is valid and to investigate related materials improvement, nondestructive testing, and the relation between laser damage, plasma initiation, and failure under stress, all initiated at small isolated spots.

I. INTRODUCTION

The thresholds of laser damage of windows, reflectors, coating, and multilayer-dielectric reflectors and the initiation of plasmas at solid surfaces occur almost universally at small isolated spots, rather than uniformally over the laser beam. Determining the source of the isolated-spot damage and plasma initiation is one of the most pressing needs of laser-damage programs. If isolated-spot damage could be eliminated, damage thresholds could be increased, by an order of magnitude or more in many cases. Equally important to understanding isolated-spot damage is understanding the role of plasmas--in the gas around the solid, in the material blown off the solid, and in the solid itself--in laser damage of materials. Boling's observations[1] of laser-damage patterns at surfaces of total internal reflection and his proposed explanation in terms of initiation of damage at very small sites may provide a major clue in understanding both isolated-spot damage and the role of plasmas in laser damage of materials.

Boling[1] observed striking characteristic laser-damage patterns at surfaces of total internal reflection. Typical damage patterns are shown in Fig. 1.1. A number of other interesting damage-morphology patterns have been observed on surfaces of laser-damaged materials. The patterns include regularly spaced straight lines, concentric circles, concentric ellipses, and points on a two-dimensional, regularly spaced lattice, in addition to the pits of characteristic shape observed by

Boling. All of these morphologies, except that of Boling, involve periodically spaced patterns. Several mechanisms for producing these patterns have been suggested, but there have been no theories to explain these effects, not even order-of-magnitude estimates. The suggested mechanisms include interference between the incident laser beam and the wave reflected from the rear surface of high-index dielectrics; generation of surface waves, either electrical or acoustical, at surface imperfections; and an unspecified non-linear interaction between two laser modes which generates a surface acoustic wave.

Of the numerous investigations of the role of plasmas in damage of solids, the following are most closely related to the present study. Boling and coworkers[2] attributed the severe damage to exit surfaces of windows to the coupling between the incident beam and that reflected from the plasma at the exit surface. Smith[3] observed a string of isolated-spot-damage sites in the bulk of window materials and suggested that microplasmas were formed at sites at which starting electrons were present and that the microplasmas could not grow to form a continuous damage track in the short, 30-ps-pulse duration. Milam[4] showed that a combination of the initiation of damage by photoionization and the spread of the damage during the pulse explained a wide variety of damage results. Bloembergen[5] suggested that field enhancement at small cracks in dielectrics could initiate breakdown. Sparks[6] suggested several sources of isolated-spot damage including initiation of damage at clusters of microscopic imperfections or impurities.

The purpose of the present study is to further develop the ideas of Boling that explain his results qualitatively and have important

general implications on the laser damage of solids. In addition to developing these ideas, which turn out to be inadequate to explain the experiments, modifications are proposed. The modified ideas, which include such effects of the electric field outside the prism as gas breakdown, may explain the observed damage, but not conclusively so at present.

The experimental results of Boling were as follows: The geometry of the incident-, reflected-, and total-fields for P and S polarizations are shown in Fig. 1.2. The samples were glass prisms. The characteristic shapes of the damage sites shown in Fig. 1.1 were observed at the surface at which total internal reflection occured. The energy density at which the damage occurs is typically 100 J/cm^2, corresponding to an irradiance of $I = 3.3$ GW/cm^2 for 30 ns pulses of 1.06 μm wavelength. If the irradiance is increased by approximately 20 percent, damage occurs at the entrance surface, rather than at the total-internal-reflection surface. (See Fig.1.2) For damage at the entrance surface, a plasma is observed, but for damage at the total-internal-reflection surface, no plasma is observed.[7] The irradiance 3.3 GW/cm^2 is a factor of $(6.2)^2$ smaller than the experimental value[8] 126 W/cm^2 that is believed to be the intrinsic electron-avalanche-breakdown value for sodium chloride with 1.06 μm, 10ns pulses. (The corresponding value for the glass is unknown.)

Milam[9] observed the same damage shapes, but of smaller size, with 1 ns pulses. A plasma was observed, as discussed in Sec. V. By using his total-internal-reflection-microscopy technique, Temple[10] observed

small sharp features at the bottoms of the shallow pits created in normal-incidence damage. These sharp features are consistent with the cores of the Boling damage sites.

II. DEVELOPMENT OF THE ORIGINAL IDEAS

In this section it is shown that the original ideas cannot explain Boling's observed damage sites. Boling noticed the striking, detailed similarity between the damage-site pattern and the angular dependence of the scattering cross section of a perfectly conducting sphere with $ka << 1$, where $k = 2\pi n/\lambda$ is the propagation vector in the medium and a is the radius of the sphere. This scattering cross section, plotted in Fig. 2.1, is derived in Jackson[11] and in Sec. IV. Boling suggested that the damage initiates with the formation of a very small plasma, which grows in size to form the core of the damage site, marked in Fig.1.1a. The scattered field from the core interferes constructively with the unperturbed field to give a total field sufficiently large to cause the damage over the whole pattern.

The first task of the current program is to provide the simplest analysis based on Boling's ideas. The source of the initial very small plasma is unknown. Possible sources of the small plasma, with general sources of isolated-spot damage and isolated-spot plasma initiation included for completness, include the following:

- macroscopic inclusions--such as embedded polishing materials, particles embedded by diamond turning, or platinum particles in laser glasses--on or under the surface,
- flakes or protusions on surfaces,
- contaminated grain boundaries, dislocations, or other areas,
- dust or other air-born contaminents on or near the surface,
- clusters of impurity ions or atoms, with the clustering resulting from accumulation of the impurities at such low energy sites as

grain boundaries, scratches, or slip surfaces, or even from statistical variations of the impurity density,

- scratches, pits, or other surface imperfections,
- contaminated scratches, pits, or imperfections,
- thermally isolated areas, such as metallic flakes on metal surfaces or an area that is thermally isolated by a bubble or inclusion just under the surface,
- Bloembergen-type or lensing-type electric-field enhancement by cracks, voids, or inclusions,
- field enhancement at non-normal-incidence areas, (the irradiance at a metallic surface for grazing incidence can be four times greater than the incidence irradiance, compared to a surface irradiance that is much, much less than the incident irradiance for normal incidence),
- thermionic emission of electrons,
- field emission of electrons, from sharp features on the surface, for example,
- plasma-initiation centers, including those listed above,
- nonabsorbing imperfections in multilayer-dielectric coatings that allow the incident field to penetrate to the absorbing substrate,
- localized oxidized, or sulfurized areas, and
- dirt.

Preliminary estimates suggest that the growth of the original plasma to a large size is easy to explain, and is not the limiting feature of the proposed theory. Possible growth mechanisms of the core plasma include electron-avalanche breakdown in the enhanced field, thermal diffusion, electron diffusion, radiation propagation of the plasma, and shock heating.

For example, growth by electron-avalanche breakdown in the near field is reasonable because the electric field at the two poles of a small, perfectly conducting sphere is three times greater than the incident field (and is even greater at the ends of a perfectly conduction ellipse or at *sharp conducting edges in general*). *The field incident on the sphere* can be twice as great as the field incident on the total-internal-reflection surface (as a result of the constructive interference of the incident and totally reflected waves). Thus, the field at the tips of even the sphere is $2 \times 3 = 6$ times greater than the field incident on the prism (at the inside of the surface, so that the charge in the field at the entrance surface need not be considered). As mentioned in Sec. I, the electron-avalanche-breakdown field for sodium-chloride is also a factor of six greater than the damage field for the glass prisms. Thus, electron-avalanche breakdown is likely.

Suppose that the core of the plasma grows to the size corresponding to $k_e a \cong 1$, where the wave vector k_e of the incident plus reflected wave from the total-internal-reflection surface is

$$k_e = k/2^{1/2} = 2^{1/2}\pi n/\lambda \quad ,$$

as discussed in Sec. III. The radius of the core plasma is then

$$a = 1/k_e = 2^{1/2}\lambda/2\pi n = 1.06\ \mu m/2^{1/2}\pi\ (1.5) = 0.16\ \mu m \quad .$$

Thermal diffusion could account for the growth because the thermal-diffusion distance is approximately equal to a:

$$\ell_{th} = (Kt/C)^{1/2} \cong [(10^{-2}\ \mathrm{W/cmK})\ 30 \times 10^{-9}\ \mathrm{s}/(2\ \mathrm{J/cm^3K})]^{1/2}$$

$$= 0.12\ \mu\mathrm{m} \quad .$$

Plasma propagation in the high fields of the near-field region is another possible source of core-plasma growth.

The energy required to form the plasma is negligible. The energy associated with a plasma temperature of 2 eV is

$$\mathcal{E}_p = \frac{4\pi}{3}(0.16 \times 10^{-4})^3\ 5 \times 10^{22}\ \frac{\text{atoms}}{\text{cm}^3}\ 2\ \frac{\text{eV}}{\text{atom}}\ 1.6 \times 10^{-19}\ \frac{\text{J}}{\text{eV}}$$

$$= 2.75 \times 10^{-10}\ \mathrm{J}\ ,$$

which is negligible with respect to the energy incident on the area πa^2

$$\mathcal{E}_{in} \cong (100\ \mathrm{J/cm^2})\,\pi\,(0.16 \times 10^{-4}\ \mathrm{cm})^2$$

$$= 8.0 \times 10^{-8}\ \mathrm{J}\ .$$

In the generation and growth of the original core plasma, it is important to realize that the absorption of small particles does not contain the well-known factor $(ka)^4$ for scattering; thus, the absorption cross section can remain reasonably large for small values of ka.

In the original model, the unperturbed field near the total-internal-

reflection surface consists of the incident field and the perpendicularly propagating reflected field. The total field is modeled formally by a plane wave propagating in an infinite medium containing a single spherical particle that is a perfect conductor. The complete field distributions, including the near field, far field, and intermediate region, for both linear polarizations and both right- and left-circular polarizations of the incident field are derived in Sec. IV. For the case of $ka \ll 1$, the results, given in Eq. (A4) of appendix A, are quite simple. The near-field distribution is simply the dipole field of a perfectly conducting sphere in a dc electric field, with the time dependence and, for circular polarization, the polarization dependence added formally. See Eq. (A6) of appendix A.

The squares of the magnitude of the far-fields for the two linear polarizations $\hat{e} = \hat{x}$ and $\hat{e} = \hat{y}$ and the two circular polarizations $\hat{e} = (\hat{x} \pm i\hat{y}) \times$ $\times 2^{1/2}$, where $\hat{e}$ is the unit vector in the direction of the electric-field, are

$$E_{sc}^2 = A[(\cos\theta - 2)^2 - 3\sin^2\theta\cos^2\phi], \qquad \text{for } \hat{e} = \hat{x}, \quad (2.1a)$$

$$E_{sc}^2 = A[(\cos\theta - 2) - 3\sin^2\theta\sin^2\phi], \qquad \text{for } \hat{e} = \hat{y}, \quad (2.1b)$$

$$E_{sc}^2 = A[\tfrac{5}{2}(1 + \cos^2\theta) - 4\cos], \qquad \text{for } \hat{e} = (\hat{x} \pm i\hat{y})/2^{1/2},$$

where

$$A = [(ka)^3 E_{inc}/2(kr)]^2 \qquad (2.2)$$

with E_{inc} the electric field incident on the sphere. These expressions are plotted in Fig. 2.2 as polar plots in the x-y plane ($\phi = 0$), that is

$$E_{sc}^2 = A[(\cos\theta - 2)^2 - 3\sin^2\theta], \qquad \text{for } S(\hat{e} = \hat{x}) \qquad (2.3a)$$

$$E_{sc}^2 = A(\cos\theta - 2)^2 \qquad \text{for } P(\hat{e} = \hat{y}) \qquad (2.3b)$$

$$E_{sc}^2 = A[\tfrac{5}{2}(1 + \cos^2\theta) - 4\cos\theta], \qquad \text{for circ. or unpol.} \qquad (2.3c)$$

The square of the far-field electric field is proportional to the differential scattering cross section $d\sigma/d\Omega$ because the magnitude of the time-average poynting vector is

$$S = n^2 E_{sc}^2 c/8\pi n \qquad (2.4)$$

and

$$\frac{d\sigma}{d\Omega} = S_{far} r^2 \Big/ \frac{n^2 E_{inc}^2 c}{8\pi n} = r^2 E_{sc}^2/E_{inc}^2 \qquad (2.5)$$

From Eqs. (2.5), (2.4) and (2.3c), the differential cross section for circular polarization is

$$d\sigma/d\Omega = a^2(ka)^2 [\tfrac{5}{8}(1 + \cos^2\theta) - \cos\theta], \qquad \text{for circ.} \qquad (2.6)$$

The angular dependence of E_{sc}^2, or equivalently $d\sigma/d\Omega$, for circular polarization or for unpolarized radiation in Eq, (2.3c) is the damage pattern observed by Boling. The pattern in Eqs. (2.3a) and (2.4b) for P- and S-linear polarizations are different from the observed damage pattern. Since the experiments were performed with linearly polarized radiation, the theoretical patterns do not agree with the experimental patterns. The disagreement between the observed and theoretical angular patterns may not be serious for S polarization because technical factors may eliminate the zero at $\theta = 60°$ in the S-polarization curve in Fig. 2.2. Indeed, the

tip of the damage pattern for S polarization at the top of Fig. 1.1(b) is more elongated than that of the P polarization at the top of Fig. 1.1(a).

A more serious difficulty with the theory is that at the great distances at which most of the damage occurs, the scattered-field amplitude is small with respect to the unperturbed-field amplitude; thus,

$$E_{tot}^2 = (E_{inc} + E_{sc})^2$$

$$\cong E_{inc}^2(1 + 2\, E_{sc}/E_{inc}) \quad . \tag{2.7}$$

The scattered-field contribution to E_{tot}^2 is linear in E_{sc}, rather than being proportional to E_{sc}^2. The patterns for E_{sc} are of course quite different from the patterns for E_{sc}^2 (and different from the observed damage pattern), as seen in Figs. 4.7 and 4.8 of Sec. IV. Thus, the original thoery does not explain the striking angular dependence of the damage pattern, as originally thought.

The third, and most serious difficulty with the original theory is that the magnitude of the scattered field is not sufficiently large to explain the results. The central results of the numerical analysis of Sec. IV are as follows: For $ka << 1$, the near-field ($kr \lesssim 1$) electric field decreases as $1/r^3$ and the far-field ($kr \gtrsim 1$) decreases as $1/r$. The magnitude of the field at all r is approximated sufficiently well for the present estimate by using the near-field results for $kr < 1$ and the far-field results for $kr > 1$. Thus, for $ka << 1$, the electric field drops to a very small value before the far-field pattern is established. For example, for $ka = 1/5$, $(E_{sc}/E_{inc})^2 \cong (1/5^3)^2 = 6.4 \times 10^{-5}$ at $kr = 1$. In order to explain the experiments, the field must be non-negligible at larger r, for which the inequality $kr >> 1$ is satisfied.

Since the observed damage pattern is the far-field pattern and the scattered field is small in the far-field region for ka << 1, scattering by small particles, with ka << 1, cannot explain the observation of Boling. The magnitude of the electric field is much larger for the case of ka $\gtrsim$ 1 than for the case of ka << 1, but the angular dependence is different for ka $\gtrsim$ 1 from that observed in the damage experiments. If the model is to explain the results, the value of ka must be as large as possible so that the scattering field is large, but small enough for the far-field pattern to be that of the observed damage pattern. The resulting maximum value of ka is somewhat less than one. As seen by comparison of Fig. 4.7 with Fig. 4.8 of Sec. IV, the far-field electric-field angular distribution for ka = 1 is quite noticeably different from the distribution for ka << 1.

Even with ka = 1 used formally in the original theory, the scattered field is still too small to explain the experimental results. Formally setting ka = 1 and $\theta = \pi$ (because the most distant part of the damage pattern occurs at $\theta = \pi$) in Eq. (2.2) and (2.3c) gives $A = (E_{inc}/2\ kr)^2$ and

$$E_{sc} = 3\ E_{inc}/2\ kr, \qquad \text{for ka = 1, circ, } \theta = \pi. \tag{2.8}$$

From Eqs. (2.8) and (2.7), the correction factor to the square of the total field is 3/kr. For λ = 1.06 μm, n = 1.5, and r = 30 μm (at the edge of a typical damage area at $\theta = \pi$), the value of 3/kr is

$$3/kr = 3(1.06)/2\pi(1.5)30 = 1.1 \times 10^{-2}\ , \tag{2.9}$$

corresponding to only a one percent increase in the irradiance. Even for the smaller observed damage sites, at a distance of 30/4 = 7.5 μm from the core, the scattered irradiance is only four percent of the unperturbed irradiance.

It is unlikely that a one to four percent increase in the irradiance would cause damage. Except for the angular dependence of the scattering in the far field, the results above were obtained from intuitive arguments and confirmed by the numerical analyses in Sec. IV.

The scattering cross section of the core can be greater than $2\pi a^2$, by factors at least as great as two, at some value of ka typically slightly greater than one. Such increased scattering cannot account for the observations. First, for $ka \geq 1$, the angular distribution is no longer the same as for $ka << 1$. Second, the magnitude of the scattered field is still too small to explain the results.

A number of other effects are of interest. The near-field electric field at the tips of an elliptical particle is greater than at the poles of the spherical particle considered above. Thus, the core plasma could grow into an elliptical shape. In general, either spherical or elliptical growth is possible, depending on the growth mechanism. The original small plasma could be either on the surface or embedded under the surface. The dark area at the core in some damage pictures has a radius of approximately 1 μm, corresponding to $ka >> 1$. As discussed above, the scattering pattern for $ka >> 1$ does not resemble the observed damage pattern. This observation does not necessarily invalidate the theory. The large core could be related to near-field excitation of the gas-breakdown plasma.

The same damage mechanism responsible for the characteristic damage-pattern shapes of Boling could be involved in the commonly observed damage at normal incidence. The damage sites are then expected to be spherical, corresponding to the end-on views of the far-field pattern. For normal incidence, for

incidence at angles less than the total-internal-reflection angle (so that there is a propagating transmitted wave), or for front-surface damage the effect of the plasmas is likely to be different from those in the case of total internal reflection because the plasma can propagate away from the surface in the former cases, as discussed in Sec. III.

III. MODIFICATION OF THE ORIGINAL IDEAS

In this section it is shown that an extension of the model in Sec. II may be able to explain the experimental results. However, the existence of the small plasma should be established experimentally and other experiments performed, and the additional analysis discussed in Sec. V should be performed in order to firmly establish the validity of the theory. The essential feature of the extended model is including effects of the scattered field outside the prism, such as gas breakdown in the small gas volume outside the total-internal-reflection surface in which the scattered field is large. The extended model also includes using the correct polarizations of the total electric field (incident-plus reflected-field at the total-internal-reflection surface), which are different from the simple linear P and S polarizations of the original model. The extended model also includes the increased value of the effective wavelength $\lambda_{eff} = 2^{1/2}\lambda/n$ resulting from the vector additions of the incident and reflective fields at the total-internal-reflection surfaces, as discussed below.

The minimum value $E_{sc\ min}$ of the scattered field in the damage region (See Fig.1.1a) is so small with respect to the unperturbed field that constructive interference is not expected to cause damage. However, $E_{sc\ min}$ is much greater than the unperturbed field outside the prism (away from the rapidly decaying field that penetrates a small distance outside the surface). In other words, at the point marked $E_{sc\ min}$ in Fig. 1.1a, the scattered field is a small pertubation inside the prism, but a large pertubation outside the prism. The scattered field outside the prism could break down the air or support a plasma in the material blown off the surface. Since E_{inc} is negligible outside the prism, $E_{tot}^2 \sim E_{sc}^2$; thus, the problem of the linearity in E_{sc} in Eq. (2.7) is eliminated.

Plasmas outside the prism will be called gas plasmas to distinguish them from the core plasma. Plasma erosion could account for the damage, either essentially all of the damage or possibly only the damage far from the core. Absorption of the visible- and ultraviolet-radiation from the plasma by the material is possible in principle, and is indeed believed to be involved in some laser-damage results well above the damage threshold. The initiation of the gas plasma could occur over the whole damage area, or the plasma could propagate outside the area in which it is ignited. Propagation from the core to the most distant point of damage (typically 8 to 30 μm from the core) would require a velocity of Mach 1 to 3. It is likely that direct breakdown, rather than breakdown plus propagation, is involved in the damage. In general, both the initiation and maintenance of the gas plasma may be important.

It would, in fact, be surprising if the gas did not break down at the damage site. When the irradiance is increased by approximately 20 percent above the value required to damage the total-internal-reflection surface, the entrance surface of the prism is damaged, and a plasma is observed. The electric field just outside the total-internal-reflection surface near the core is expected to be greater than the field just outside the entrance surface. First, the unperturbed field inside the prism near the total-internal-reflection surface is two times greater than the electric field in the prism just inside the entrance surface in the usual case in which the beam is sufficiently small in diameter that the reflected beam does not overlap the incident beam at the entrance surface of the prism. Furthermore, the near-field electric field (unperturbed plus scattered) is three times greater than the unperturbed field at the two ends of the sphere (along

the direction of the electric field). With these two factors, the irradiance in the prism is up to $(2 \times 3)^2 = 36$ times greater than the irradiance inside the prism at the entrance surface.

Furthermore, the gas breakdown thresholds of clean air at 1.06 um for 40 ns pulses (the closest value to the 30 ns pulses of Boling) is 100 GW/cm^2, which is a factor of 30 greater than the irradiance incident on the entrance surface. The breakdown of laboratory air, which is assumed to be dirty in gas breakdown studies, occurs at much lower irradiance than that of clean air in general, and the breakdown of gases in the presence of surfaces is lower than the breakdown far from surfaces. Again, gas breakdown is expected to occur at or near the irradiance level at which the damage is observed.

The very sharp and regular edges of the outline of the damage pattern, with no trace of interference patterns, is consistent with a gas-plasma phenomena. The gas could conceivably be ionized at great distance from the surface, where the electric field is small, by shock-wave propagation and plasma ignition. Such shock-wave initiation is unlikely because shock ionization usually is important at values of irradiance greater than those of the present experiments. Contamination of the surface of the prism could be involved, but not necessarily so.

The unperturbed fields inside the total-internal-reflection surface are easy to derive. From pages 219-221 of Jackson, Classical Electrodynamics,[11] the incident- and reflected-electrical fields for the case of total-internal-reflection are

$$\underset{\sim}{E} = \underset{\sim}{E}_{inc}\, e^{i\underset{\sim}{k}_{inc}\cdot\underset{\sim}{r} - i\omega t} \qquad (3.1)$$

and

$$\underset{\sim}{E} = \underset{\sim}{E}_{ref}\, e^{i\underset{\sim}{k}_{ref}\cdot\underset{\sim}{r}}\, e^{-i\omega t} \tag{3.2}$$

where

$$\underset{\sim}{k}_{inc} = \hat{x}\, k_x + \hat{z}\, k_z \tag{3.3}$$

and

$$\underset{\sim}{k}_{ref} = -\hat{x}\, k_x + \hat{z}\, k_z \tag{3.4}$$

with

$$k_x = 2\pi n \cos\theta_i/\lambda, \qquad k_z = 2\pi n \sin\theta_i$$

$$k_x = k_z \equiv k_e = 2\pi n/2^{1/2}\lambda \quad , \qquad \text{at } \theta_i = \pi/4 \quad , \tag{3.5}$$

with n the index of refraction of the prism, θ_i the angle of incidence. The index of refraction of the medium outside the prism equal to one.

For S polarization (electric field in tne plane of the reflecting surface as shown in Fig. 1.2),

$$\underset{\sim}{E}_{inc} = \hat{y}\, E_{inc}, \qquad \underset{\sim}{E}_{ref} = \hat{y}\, e^{i2\phi_S} E_{inc}, \qquad \text{S pol.} \tag{3.6}$$

where

$$\phi_S = -\tan^{-1}[(n^2 \sin^2\theta_i - 1)^{1/2}/n\cos\theta_i] \,. \tag{3.7}$$

The expression for ϕ_S in Eq. (3.7) is obtained from Jackson's results

$$\frac{E_{ref}}{E_{inc}} = -\frac{\sin(\theta_i - \theta_r)}{\sin(\theta_i + \theta_r)}, \qquad \text{S pol.} \qquad (3.8)$$

$$\sin\theta_r = n \sin\theta_i \qquad (3.9)$$

$$\cos\theta_r = i\,(n^2 \sin^2\theta_i - 1)^{1/2} \qquad (3.10)$$

and

$$\sin(\theta_i \pm \theta_r) = \sin\theta_i \cos\theta_r \pm \cos\theta_i \sin\theta_r . \qquad (3.11)$$

For P polarization (electric field perpendicular to both $\underset{\sim}{k}_{inc}$ and $\underset{\sim}{E}$ for S polarization, as shown in Fig. 1.2),

$$\underset{\sim}{E}_{inc} = (-\hat{x} + \hat{z})\, E_{inc}/2^{1/2}, \qquad \text{P pol.}, \qquad (3.12)$$

$$\underset{\sim}{E}_{ref} = (-\hat{x} - \hat{z})\, E_{inc}\, e^{i2\phi_p}/2^{1/2}, \qquad \text{P pol.}, \qquad (3.13)$$

where

$$\phi_p = -\tan^{-1}[(n^2 \sin^2\theta_i - 1)^{1/2}/n \sin\theta_i] - \tan^{-1}[(n^2 \sin^2\theta - 1)^{1/2} \cos\theta_i/n \sin^2\theta_i] \qquad (3.14)$$

The expression for ϕ_p in Eq. (3.14) is obtained from Eqs. (3.9), (3.10), (3.11), and Jackson's result

$$\frac{E_{ref}}{E_{inc}} = \frac{\tan(\theta_i - \theta_r)}{\tan(\theta_i + \theta_r)}, \qquad \text{P pol.} \qquad (3.15)$$

The total fields (incident plus reflected) obtained by adding $\underset{\sim}{E}_{inc}$ and $\underset{\sim}{E}_{ref}$ in Eqs. (3.1) and (3.2) and using Eqs. (3.3), (3.4), (3.6), (3.12), and (3.13) are

$$\underline{E}_S = \hat{y}\, 2E_{inc}\, e^{ik_z z}\, e^{i\phi_S} \cos(k_x x - \phi_S) \qquad (3.16)$$

$$\underline{E}_p = 2^{1/2} E_{inc}\, e^{ik_z z}\, e^{i\phi_p} [-\hat{x} \cos(k_x x - \phi_p) + i\hat{z} \sin(k_x x - \phi_p)] \,. \qquad (3.17)$$

These results in Eqs. (3.16) and (3.17) for the total unperturbed fields show the following: The wavelength for $\theta_i = \pi/4$,

$$\lambda_e = 2\pi n/k_e \,, \qquad (3.18)$$

of the total field is $2^{1/2}$ times longer than that of the incident field alone, as seen from Eq. (3.5) and (3.18). Both the S and P waves propagate along the z axis [$E \sim \exp(ik_z z)$]. The x dependence for S polarization is a standing wave whose phase at the surface is ϕ_S and whose wavelength is $\lambda_x = 2\pi/k_x = \lambda/n \cos\theta_i$. The x dependence for P polarization is a wave that changes from x polarization to circular polarization to z polarization to circular in the opposite sense as x increases. The phase of the E vector in the x-z plane at the x = 0 surface is ϕ_p and the wavelength of the x variation is $\lambda_x = 2\pi/k_x = \lambda/n \sin\theta_i$. The circular polarization is quite different from the usual transverse circular polarization of a plane wave. In Eq. (3.17), one component (z) of the circular polarization is longitudinal. In other words, the plane of polarization contains the propagation vector $k_z\hat{z}$.

IV. SCATTERING FROM A PERFECTLY CONDUCTING SPHERE

A Fortran program, which we call SPHERSCAT, was written to compute the total field (incident plus scattered) from a monochromatic linearly polarized plane wave incident on a perfectly conducting sphere of radius a. Following Jackson,[11] the total field is written

$$\underline{E}(\underline{r}) = E_{inc} e^{ikz\hat{x}} + \underline{E}_{sc}(\underline{r}) \tag{4.1}$$

where $E_{inc} e^{ikz\hat{x}}$ represents the incident field polarized along the x axis propagating in the z direction and the scattered field is

$$E_{sc} = E_{sc}^{(+)} + E_{sc}^{(-)} \quad , \tag{4.2}$$

where

$$\underline{E}_{sc}^{(\pm)}(\underline{r}) = \frac{E_{inc}}{4} \sum_{\ell=1}^{\infty} i^{\ell} \sqrt{4\pi(2\ell+1)} \left[\alpha_{\pm}(\ell) h_{\ell}^{(1)}(kr) \underline{X}_{\ell,\pm 1}(\theta,\phi) \right.$$

$$\left. \pm \frac{\beta_{\pm}(\ell)}{k} \nabla \times h_{\ell}^{(1)}(kr) \underline{X}_{\ell,\pm 1}(\theta,\phi) \right] \tag{4.3}$$

are the scattered fields for right- and left-circular polarized incident fields. The Hankel functions $h^{(1)}$ and $h^{(2)}$ and the vector spherical harmonics $\underline{X}_{\ell,\pm 1}$ are discussed below, and the parameters $\alpha_{\pm}(\ell)$, $\beta_{\pm}(\ell)$ are defined as

$$\alpha_{\pm}(\ell) = -\left[\frac{h_{\ell}^{(2)}(ka)}{h_{\ell}^{(1)}(ka)} + 1 \right], \quad \beta_{\pm}(\ell) = -\left[\left. \frac{\frac{d}{dr}(rh_{\ell}^{(2)}(kr))}{\frac{d}{dr}(rh_{\ell}^{(1)}(kr))} \right|_{r=a} + 1 \right] \tag{4.4}$$

SPHERSCAT evaluates Eq. (4.3) for arbitrary $\underline{r}$ by computing terms in the series up to $\ell = \ell_{max}$ determined by the magnitude of $u \equiv ka$. The Hankel functions are computed recursively using the relations

$$h_{\ell+1}(u) = \frac{2\ell+1}{u} h_\ell(u) - h_{\ell-1}(u) \quad , \tag{4.5a}$$

$$\frac{d}{du}(uh_\ell) = uh_{\ell-1}(u) - \ell h_\ell(u) \quad , \tag{4.5b}$$

and initializing the calculation with the definitions

$$h_1^{(1)}(u) = \frac{-e^{iu}}{u}\left(1 + \frac{i}{u}\right) \quad , \; h_2^{(1)}(u) = \frac{ie^{iu}}{u}\left(1 + \frac{3i}{u} - \frac{3}{u^2}\right) \tag{4.6a}$$

$$\frac{d}{du}\left(uh_1^{(1)}\right) = e^{iu}\left(-i + \frac{1}{u} + \frac{i}{u^2}\right) \quad , \; \frac{d}{du}\left(uh_2^{(1)}\right) = e^{ix}\left(-1 - \frac{3i}{u} + \frac{6}{u^2} + \frac{6i}{u^3}\right). \tag{4.6b}$$

Evaluation of Eqs. (4.5) and (4.6) for $u = ka$, $1 \le \ell \le \ell_{max}$, provides the coefficients $\alpha_{\pm}(\ell)$, $\beta_{\pm}(\ell)$. Numerical evaluation of Eq. (4.3) was performed by first expanding the curl in the second term as

$$\nabla \times h_\ell^{(1)}(kr)\, \underset{\sim}{X}_{\ell,\pm 1} = i\hat{n}\, \frac{\sqrt{\ell(\ell+1)}}{r}\, h_\ell^{(1)}(kr)\, Y_{\ell,\pm 1} + \frac{1}{r}\frac{\partial}{\partial r}\left(rh_\ell^{(1)}(kr)\right) \hat{n} \times \underset{\sim}{X}_{\ell,\pm 1} \; . \tag{4.7}$$

This relation follows from Jackson Eq. (16,143). Using Eqs. (4.5) through (4.7) provides the required radial dependencies. Due to the use of forward recursion relations, Eq. (4.5) are useful only for $\ell_{max} \le 20$; beyond this value numerical roundoff becomes a problem. The same holds for the spherical harmonics $Y_{\ell m}$, to be discussed next.

The spherical harmonics $Y_{\ell m}$ are defined with Jackson's phase choice as

$$Y_{\ell m}(\theta,\phi) = \left[\frac{2\ell + 1}{4\pi} \frac{(\ell - m)!}{(\ell + m)!}\right]^{1/2} P_\ell^m(\cos\theta) e^{im\phi} \tag{4.8}$$

where the associated Legendre functions are obtained recursively from the expression

$$P_{\ell+1}^m(\cos\theta) = \frac{(2\ell + 1)\cos\theta\, P_\ell^m - (\ell + m)P_{\ell-1}^m}{\ell - m + 1} \tag{4.9}$$

For the calculation at hand, only $|m|$ values less than two are required. The recursion is initialized with

$$P_1^0 = \cos\theta, \quad P_1^1 = \sin\theta, \quad P_1^2 \equiv 0 \ , \tag{4.10a}$$

$$P_2^0 = \frac{1}{2}(3\cos^2\theta - 1), \quad P_2^1 = -3\sin\theta\cos\theta, \quad P_2^2 = 3\sin^2\theta \ . \tag{4.10b}$$

Equations (4.8) through (4.10) provide $Y_{\ell m}$ for positive m; negative m values are obtained from the expression

$$Y_{\ell,-m}(\theta,\phi) = (-1)^m Y_{\ell m}^*(\theta,\phi) \ . \tag{4.11}$$

To complete the calculation, the vector spherical harmonics $\underset{\sim}{X}_{\ell m}$ for $m = \pm 1$ are constructed using the definition

$$\underset{\sim}{X}_{\ell m} = \frac{1}{\sqrt{\ell(\ell + 1)}} \underset{\sim}{L} Y_{\ell m} \ , \tag{4.12}$$

where the differential operator $\underset{\sim}{L} = -i\hat{r} \times \nabla$. Using the raising and lowering operators $L_\pm$, the following explicit expressions for $\underset{\sim}{X}_{\ell,\pm 1}$ are obtained

$$\chi_{\ell,\pm 1} = \frac{1}{\sqrt{\ell(\ell+1)}}\left[\frac{1}{2}\left(\sqrt{(\ell \mp 1)(\ell+1\pm 1)}\, Y_{\ell,1\pm 1} + \sqrt{(\ell \pm 1)(\ell+1\mp 1)}\, Y_{\ell,-1\pm 1}\right),\right.$$

$$\frac{1}{2i}\left(\sqrt{(\ell \mp 1)(\ell+1\pm 1)}\, Y_{\ell,1\pm 1} - \sqrt{(\ell \pm 1)(\ell+1\mp 1)}\, Y_{\ell,-1\pm 1}\right),$$

$$\left. \pm Y_{\ell,\pm 1}\right]. \qquad (4.13)$$

In practice, values of ka, ℓ_{max}, and a range of values of kr, θ, ϕ are input into the program, which first computes $\alpha_{\pm}(\ell)$, $\beta_{\pm}(\ell)$. SPHERSCAT next computes an array of Hankel functions and their derivatives for $1 \le \ell \le \ell_{max}$ for each kr value. The spherical harmonics are computed and stored in complex arrays for each ℓ and $m = \pm 1$ for each set of spherical angles (θ,ϕ). The stored results are combined according to Eqs. (4.1), (4.2) and (4.3) to produce the electric field. The resulting magnitude is then listed and plotted either for fixed kr, continuous θ, $0 \le \theta \le \pi$, and fixed ϕ or for θ,ϕ fixed and continuous kr. Results of the program have been checked against hand-calculator computations for ℓ up to 2. Since the same equations are used beyond $\ell = 2$ it is felt the program is reliable for moderate ℓ_{max} values. For large ℓ_{max} values needed for ka >> 1 the multipole series here should, of course, be replaced by an asymptotic series whose first term gives the isotropic result described in Jackson, Sec. 9.10.

The program SPHERSCAT was used to study the angular and radial dependence of scattered and total radiation fields produced by small spherical conductors. First it was verified that the program gives the correct results for the near- and far-field limits for the case ka << 1. For the near-zone field (kr << 1), approximate evaluation of the first term in Eq. (4.3) gives

$$\underline{E}(\underline{x}) = E_{inc}\ (\hat{x} + (a/r)^3\ [3\ \hat{r}\ \sin\theta\ \cos\phi - \hat{x}] \qquad (4.14)$$

where $\hat{r}$ is the unit vector in direction of $\underline{r}$. Derivation of this result is sketched in the appendix. Figures 4.1-4.3 show the angular dependence of $|\underline{E}|/E_{inc} = (\underline{E} \cdot \underline{E}^*)^{1/2}/E_{inc}$ computed for ka = 0.01 and kr = 0.01, 0.02, and 0.1 respectively. The radiation angular pattern in the x-z plane plotted in Fig.4.1 shows that the total field vanished in the y-z plane and is three times greater than the incident field along the ±x axes. Figures 4.2 and 4.3 show both x-z ($\phi = 0$) and y-z ($\phi = \pi/2$) plane patterns, which are similar for this case of kr = 0.1. Comparison of SPHERSCAT results with Eq. (4.14) shows excellent agreement. The near-field, dipole pattern seen for kr = 0.01 evolves quickly into the spherically symmetric pattern of the initial field alone as kr increases because the field falls off as $1/r^3$ in the near-field region.

Figure 4.4 illustrates this radial dependence by plotting $|\underline{E}_{sc}|/E_{inc}$ as a function of kr on a log scale, again for ka = 0.01 with $\theta = \pi/2$ and $\phi = 0, \pi/2$ corresponding to $\hat{x}$ and $\hat{y}$ directions. The inverse-cube dependence is maintained up to kr = 1. For kr > 1, the field smoothly and rapidly attains the asymptotic 1/r dependence. As described in the appendix, for kr >> 1 the first term in Eq. (4.3) produces the far-field electric field.

$$\underline{E}_{sc} \approx \frac{E_{inc}}{2}\ \frac{(ka)^3}{kr}\ e^{ikr}[(\hat{x}\cos\theta - \hat{z}\sin\theta\cos\phi) + 2(\hat{r}\sin\theta\cos\phi - \hat{x})]$$

$$\approx \frac{E_{inc}}{2}\ \frac{(ka)^3}{kr}\ e^{ikr}[\hat{x}(\cos\theta - 2 + 2\sin^2\theta\cos^2\phi) + \hat{y}\ 2\sin^2\theta\sin\phi\cos\phi$$

$$+ \hat{z}\sin\theta\cos\phi\ (2\cos\theta - 1)] \qquad (4.15)$$

which has the expected inverse kr behavior seen in Fig. 4.4 for kr $\geq$ 1.

To illustrate the angular pattern in the far field, we plot $|E_{sc}|/E_{inc}$, rather than $|\underline{E}|/E_{inc}$ because the scattered field is much smaller than the incident field. Figures 4.5-4.7 show the angular dependence in the x-z and y-z planes for ka = 0.01 and kr = 0.01, 1.0, 100, respectively; the case of kr = 0.01 is included for comparison. Finally, Fig. 4.8 shows the angular patterns for kr = 100 with ka = 1. Comparing Figs. 4.7 and 4.8 indicates that increasing the sphere size tends to decrease the relative backscatter and make the patterns more isotropic. As ka becomes much greater than one, we expect the patterns to become totally isotropic in the far field. The squares of $|E_{sc}|/E_{inc}$ corresponding to $|E_{sc}|/E_{inc}$ in Fig. 4.7 are plotted in Fig. 2.2, which also contains the result for circular polarization (or unpolarized radiation).

The motivation for this study was to examine the conditions needed to produce radiation patterns in Fig. 2.1. Although it is possible to achieve scattered radiation fields having the desired form by making ka $\ll$ 1 and kr $\gg$ 1 simultaneously, the total field will be close to the incident value because of the overall small amplitude of the scattered component. Thus, some other mechanism must be considered to explain the observed damage patterns.

V. SUGGESTED ADDITIONAL INVESTIGATIONS

Analysis of the total fields in the presence of both the surface and the scattering sphere, using the correct unperturbed field rather than the plane-wave fields used in the approximate model in Sec. II would be difficult and costly. However, it is possible that a much simpler analysis could give results that are sufficiently accurate to establish the validity of the theory. First, the scattering of the more-complicated (non-plane-wave) field distribution $\underset{\sim}{E} = \underset{\sim}{E}_{inc} + \underset{\sim}{E}_{ref}$ in Sec. V could probably be obtained rather easily by using the plane-wave results of Sec. IV and superposition, with care taken in adding components and accounting for phases, angles, and the position of the scatterer. This analysis would give the scattered field for a sphere far from the surfaces of the prism.

Obtaining the scattered field outside the prism would be more difficult. As a zeroth approximation, the infinite-medium results could be used formally outside the prism. As a better approximation, a solution to the problem of a hemisphere of perfect metal on the surface or to the problem of a sphere of perfect metal halfway-embedded in the surface could be sought. It is not known how difficult this analysis would be until the problem is set up. Using ray tracing and Snell's law is not expected to give reliable results because the relevant dimensions are not large with respect to the wavelength.

The anticipated results of such further investigations are as follows: The amplitude of the scattered field obtained from the

solutions discussed above is expected to be approximately the same as the amplitudes obtained in Sec. II,III, and IV, which are marginally large enough to explain the experimental results if a plasma is ignited outside the prism. The infinite-medium results (for the sphere far from the total-internal-reflection surface, but with both the incident and reflected waves from that surface incident on the sphere) should show the observed damage pattern if the theory is to be viable. However, it is possible, though unlikely, that the presence of the surface is necessary to obtain the observed angular pattern.

It should be determined experimentally whether there is a plasma in the gas outside the total-internal-reflection surface. No plasma was observed in Boling's experiment. In similar experiments by Milam[3], a plasma was observed, but it is not known whether the plasma was in the gas, on the surface, or within the prism. The gas plasma could have gone unidentified in Boling's experiments because the plasma would not grow by propagating up the laser beam as it does in the usual damage experiments in which the electric field is large at great distances from the damaged surface. In addition to the small spatial extent of the plasma, which is confined to the regions of large scattered field, the interaction of the plasma with the surface may affect the temperature and other properties of the plasma. The surface/plasma interaction could be quite different in the total-internal-reflection experiments than in normal-incidence experiments because the plasma remains close to the surface in the total-internal-reflection case, whereas it propagates away from the surface in normal-incidence cases. N. Boling[12] believes that the plasma may not have been detected in his experiments in which the usual technique of edge-view photographs for

detecting the propagated plasma plume was used. Boling also pointed out that both he and David Milam had observed previously unexplained glows at the damage surface.

Other experiments would be useful. The effect of varying the pulse duration, wavelength, and particularly the angle of incidence and of preforming the damage experiments in vacuum and in gases other than air would be useful. All of these experiments would give useful information for determining the validity of the proposed modified theory or perhaps in suggesting a new model or further modification of the present model. Detection of the scattered field outside of the prisms before damage occurs would be an important verification of the theory and could afford a method of nondestructive testing.

Temple[10] observed surface imperfections by viewing with a microscope a surface at which there is total internal reflection in the material below the observed surface. The surface is black except in areas at which light is scattered from imperfections on or under the surface. It is possible that the total-internal-reflection surface-inspection technique of Temple could be used to advantage. However, the core plasmas would not be present at the low irradiance levels at which Temple's measurements are ordinarily made. The scattering at the small sites at which the core plasma initiates is expected to be much smaller than the scattering from the core plasma. However, it would be useful to examine the surfaces before they are damaged (as well as after damage) because Temple showed that features a few thousand nanometers in extent are visible. In addition, it would be of interest to increase the irradiance in Temple-type experiments to a sufficiently

great value that the core plasma is fully formed but sufficiently small that breakdown does not occur. The technical problems of attaining the required value of irradiance may be extremely difficult.

Preliminary results of Milam indicate that the damage sites at 1 ns are similar in shape to those of Boling at 30 ns, but are smaller in size. This is the expected behavior. The small size could result from smaller cores (from less growth, for example) or from the short time available for the gas-plasma effects to develop.

A successful theory of the extended model would be extremely important for the following reasons: laser-damage experiments are still of great interest; the role of the plasmas in laser damage is of ever increasing interest; it may be possible to develop a method of nondestructive testing; and material improvement could result from identification and removal or pacification of the damage-initiation sites. It is conceivable, although somewhat unlikely, that improving the damage resistance could also increase the strength of the material because the localized source of laser-damage initiation could be the source of failure under stress.

At Boling's suggestion, Boling, Gunther, Milam, and Sparks will meet at the Boulder Damage Symposium to discuss experiments that Gunther's students can perform.

VI. ACKNOWLEDGEMENTS

Helpful conversations with N. Boling, D. Milam, and H. Lowdermilk are gratefully acknowledged. R. Warren performed the numerical analyses and D. Mills derived the expressions for the near- and far-fields.

Appendix A

NEAR- AND FAR-ZONE EXPRESSIONS FOR SMALL SPHERES

In the limit $ka \ll 1$ Eq. (4.4) gives

$$\alpha_{\pm}(\ell) \simeq \frac{2i(ka)^{2\ell+1}}{(2\ell+1)[(2\ell-1)!!]^2}, \quad \beta_{\pm}(\ell) \simeq \frac{2i(\ell+1)(ka)^{2\ell+1}}{\ell(2\ell+1)[(2\ell-1)!!]^2} \tag{A1}$$

where $(2\ell-1)!! \equiv (2\ell-1)(2\ell-3)\ldots(3)(1)$. Retaining only the $\ell = 1$ component in Eq. (4.3) and using Eq. (4.7) produces

$$\underline{E}_{sc}(\underline{x}) \simeq -E_{inc}\left(\frac{\pi}{3}\right)^{1/2}(ka)^3\left[h_1^{(1)}(kr)\,\underline{X}_{1,\pm1} \pm 2\left(i\,\hat{r}\,\sqrt{2}\,\frac{h_1^{(1)}(kr)}{kr}\,Y_{\ell,\pm1} + \frac{1}{kr}\,\frac{\partial}{\partial r}\left(rh_1^{(1)}\right)\hat{r}\times\underline{X}_{\ell,\pm1}\right)\right]. \tag{A2}$$

From Eq. (4.8), (4.10), (4.13)

$$Y_{1,\pm1}(\theta,\phi) \simeq \mp\left(\frac{3}{8\pi}\right)^{1/2}\sin\theta\, e^{\pm i\phi} \tag{A3a}$$

$$X_{1,\pm1} = \left(\frac{3}{16\pi}\right)^{1/2}\left[(\hat{x} \pm i\,\hat{y})\cos\theta - \hat{z}\sin\theta\, e^{\pm i\phi}\right]. \tag{A3b}$$

Substitution into Eq. (A2) gives

$$\underline{E}_{sc}(\underline{x}) = \underline{E}^{+}_{sc} + \underline{E}^{-}_{sc}$$

$$= - E_{inc} (ka)^3 \left[\frac{1}{2} h_1^{(1)}(kr)(\hat{x} \cos\theta - \hat{z} \sin\theta \cos\phi) + 2i\, \hat{n}\, \frac{h_1^{(1)}(kr)}{kr} \sin\theta \cos\phi + \frac{i}{kr} \frac{\partial}{\partial r}\left(r h_1^{(1)}(kr) \right) (\hat{x} - \hat{r} \sin\theta \cos\phi)\right] \qquad \text{(A4)}$$

where $h_1^{(1)}(x) = - e^{ix}(1 + i/x)/x$ from Eq. (6a) of Sec. IV.

In the near zone $kr << 1$ and Eq. (4.6) becomes

$$h_1^{(1)}(kr) \simeq -i/(kr)^2 \quad , \frac{\partial}{\partial r}\left(r h_1^{(1)} \right) \simeq i/(kr)^2 \quad , kr << 1 \quad . \qquad \text{(A5)}$$

In this limit Eq. (A4) is dominated by the second and third terms giving

$$\underline{E}_{sc}(\underline{x}) \simeq E_{inc} (a/r)^3 (3 \hat{r} \sin\theta \cos\phi - \hat{x}) \quad , kr << 1 \quad . \qquad \text{(A6)}$$

In the far zone $kr >> 1$ and the Hankel Functions become

$$h_1^{(1)}(kr) \simeq -e^{ikr}/kr \quad , \frac{\partial}{\partial r}\left(r h_1^{(1)} \right) \simeq -i\, e^{ikr} \quad , kr >> 1. \qquad \text{(A7)}$$

The far zone limit of Eq. (A4) has contributions from the first and third terms giving

$$\underline{E}_{sc}(\underline{x}) \cong \frac{E_{inc}}{2} \frac{(ka)^3}{kr} e^{ikr} [(\hat{x} \cos\theta - \hat{z} \sin\theta \cos\phi) + 2(\hat{r} \sin\theta \cos\phi - \hat{x})]$$

$$\cong \frac{E_{inc}}{2} \frac{(ka)^3}{kr} e^{ikr} [\hat{x}(\sin^2\theta \cos^2\phi + \cos\theta - 1) + \hat{y}(\sin^2\theta \cos\phi \sin\phi)$$

$$+ \hat{z}(\sin\theta \cos\theta \cos\phi)] ,$$

$$\text{for } kr >> 1 . \qquad \underline{(A8)}$$

REFERENCES

1. N. Boling, Annual meeting of the Optical Society of America, Rochester, NY, 1979. [Norm, is this reference correct?]
2. N. Boling et. al., Applied Optics 12, 650 (1973).
3. W. L. Smith, J. H. Bechtel, and N. Bloembergen, "Picosecond Breakdown Studies: Threshold and Nonlinear Refractive Index Measurements and Lamage Morphology," NBS Spec. Publ. 435, 7th NBS-ASTM-ONR-ERDA-DARPA Symposium on Laser Damage in Optical Materials, Boulder, CO, July 29-31, 1975.
4. D. Milam, "Can a Model Which Describes Gas Breakdown also Describe Laser Damage to the Bulk and Surfaces of Solid Dielectrics," NBS Spec. Publ. 462, 8th NBS-ASTM-ONR-ERDA-DARPA Symposium on Optical Materials for High Power Lasers, Boulder, CO, July 13-15, 1976.
5. N. Bloembergen, reference to come.
6. M. Sparks, "Optical Distortion and Failure in High-Power Reflectors," Proc. High-Power Laser Optical Components and Component Material Meeting, Boulder, CO, October 3-4, 1977.
7. In subsequent experiments by Milam (private communication 1980), a plasma was observed, as discussed in Sec. V.
8. A. A. Manenkov, "New Results on Avalanche Ionization as a Laser Damage Mechanism in Transparent Solids," NBS Spec. Publ. 509, 9th NBS-ASTM-ONR-ERDA-DARPA Symposium on Laser Induced Damage in Optical Materials, Boulder, CO, Oct. 4-6, 1977, p. 455.
9. D. Milam, private communication, 1980.

10. P. A. Temple, NBS Spec. Publ. 568, Laser Induced Damage in Optical Materials, 1979, p. 333.

11. J. D. Jackson, "Classical Electrodynamics," 1st ed., John Wiley, New York, 1962.

12. N. Boling, private communication, 1980.

FIGURE CAPTIONS

Fig. 1.1. Damage morphology for: (a) P polarization and (b) S polarization. Courtesy of Dr. N. Boling.

Fig. 1.2. Geometry of the incident-, reflected-, and total-fields on the surface at which total internal reflection occurs, also showing the total fields (incident plus reflected) $\underset{\sim}{E}_p$ and $\underset{\sim}{E}_s$ for the original theory. See Sec. III for the correct $\underset{\sim}{E}_p$.

Fig. 2.1. Angular dependence of the scattering cross section (far-field irradiance) for circular polarization or unpolarized radiation, showing the same shape as the damage sites in Fig. 1.1.

Fig. 2.2. Far-field ($kr \gg 1$) scattering from a small ($ka \ll 1$) perfectly conducting sphere for different polarizations.

Fig. 4.1. Near-field angular dependence of total electric field $|\underset{\sim}{E}|/E_{inc}$ at the surface of the sphere in x-z plane for $ka = 0.01$, and $kr = 0.01$.

Fig. 4.2. Angular dependence of total electric field $|\underset{\sim}{E}|/E_{inc}$ in x-z and y-z planes for $ka = 0.01$, $kr = 0.02$, showing the great difference in the pattern for $r = 2a$ than for $r = a$ in Fig. 4.1.

Fig. 4.3. Angular dependence of total electric field $|\underset{\sim}{E}|/E_{inc}$ in x-z and y-z planes for $ka = 0.01$, $kr = 0.10$, showing the negligible scattered field for $r = 10a$ in the case of $kr \ll 1$.

Fig. 4.4. Radial dependence of scattered electric field $|\underset{\sim}{E}_{sc}|/E_{inc}$ in $\hat{x}$ and $\hat{y}$ directions for ka = 0.01, showing $E \sim 1/r^2$ for kr < 1 and $E \sim 1/r$ nominally for kr > 1.

Fig. 4.5. Near-field angular dependence of scattered electric field $|\underset{\sim}{E}_{sc}|/E_{inc}$ at the surface of the sphere in x-z and y-z planes for ka = 0.01, kr = 0.01. The corresponding total field for $\phi = 0$ is shown in Fig. 4.1.

Fig. 4.6. Angular dependence of scattered electric field $|\underset{\sim}{E}_{sc}|/E_{inc}$ in x-z and y-z planes for ka = 0.01, kr = 1, showing the small magnitude E_{sc} and the deviation from the shape for kr << 1 in Fig. 4.5 for the case of kr = 1.

Fig. 4.7. Far-field angular dependence of scattered electric field $|\underset{\sim}{E}_{sc}|/E_{inc}$ in x-z and y-z planes for ka = 0.01, kr = 100, showing the characteristic shape of the scattered field in the far field and the small magnitude of E_{sc} for kr >> 1 and ka << 1.

Fig. 4.8. Angular dependence of scattered electric field $|\underset{\sim}{E}_{sc}|/E_{inc}$ in x-z and y-z planes for ka = 1, kr = 100, showing the deviation of the shape of the pattern from that for ka << 1 in Fig. 4.7 and the greater magnitude of E_{sc} for ka = 1 than for ka = 0.01 in Fig. 4.7.

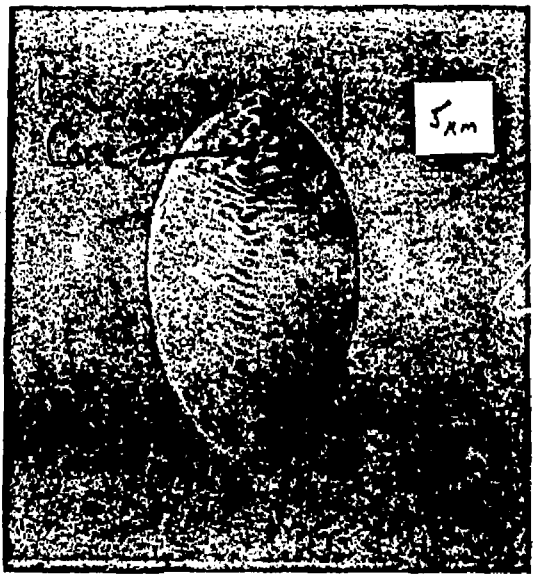

(a) P polarization

Fig. 1.1 (part 1)

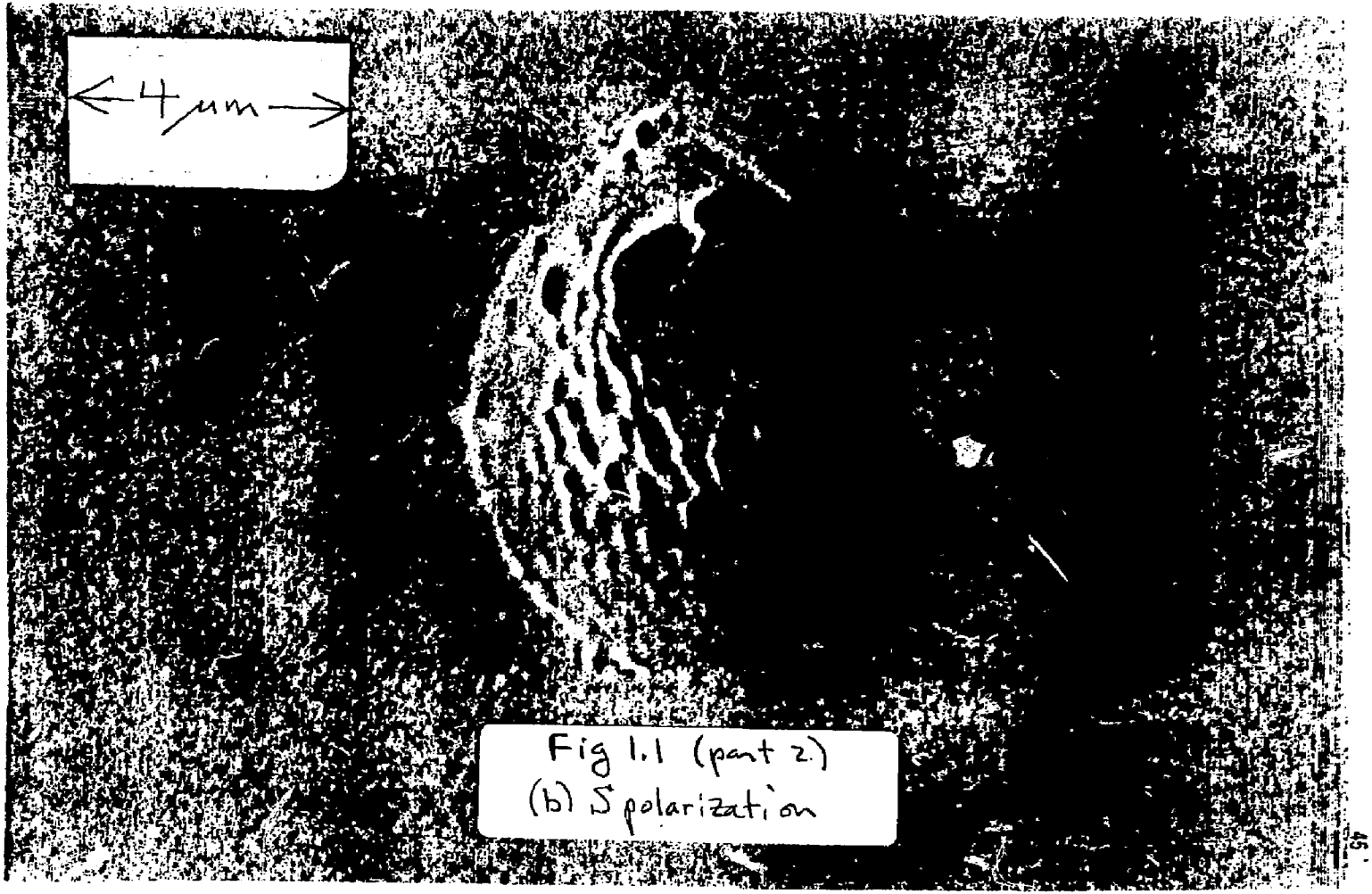

Fig 1.1 (part 2.)
(b) S polarization

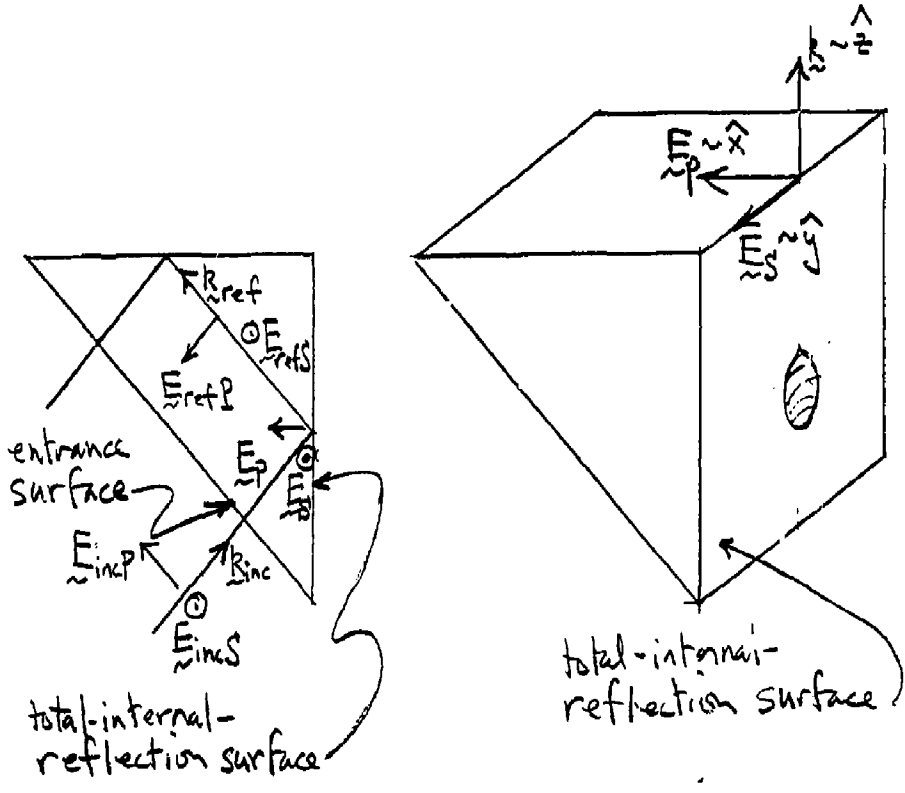
$\tilde{k}_{ref}$
$\odot \tilde{E}_{refS}$
$\tilde{E}_{refP}$
entrance surface
$\tilde{E}_P$
$\odot \tilde{E}_{PR}$
$\tilde{E}_{incP}$
$\tilde{k}_{inc}$
$\odot \tilde{E}_{incS}$
total-internal-reflection surface
(a)
$\tilde{k} \sim \hat{z}$
$\tilde{E}_P \sim \hat{x}$
$\tilde{E}_S \sim \hat{y}$
total-internal-reflection surface
(b)

Fig. 1.2.

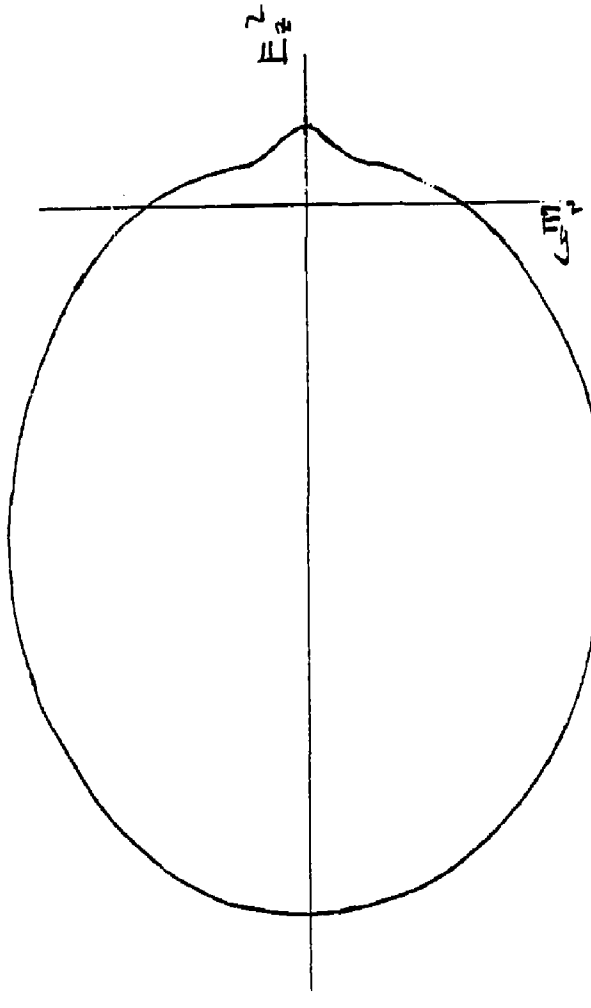

Fig. 2.1

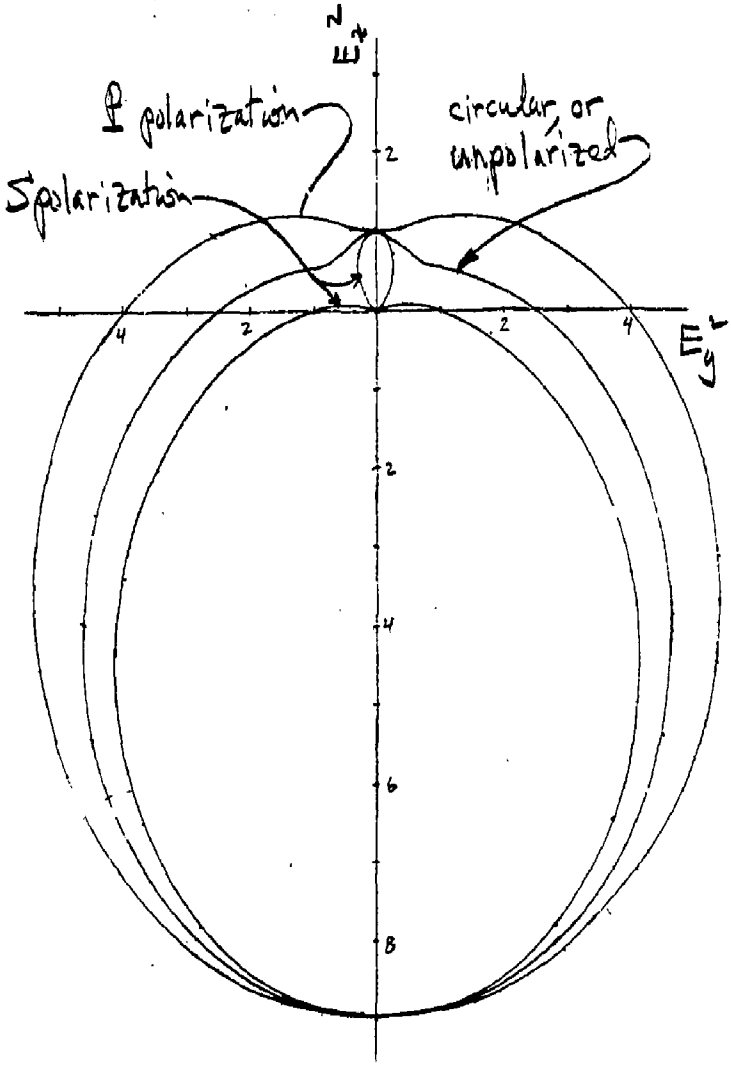
N
W
E
S
f polarization
S polarization
circular or
unpolarized
2
4
2
2
4
2
4
6
8

Fig. 2.2

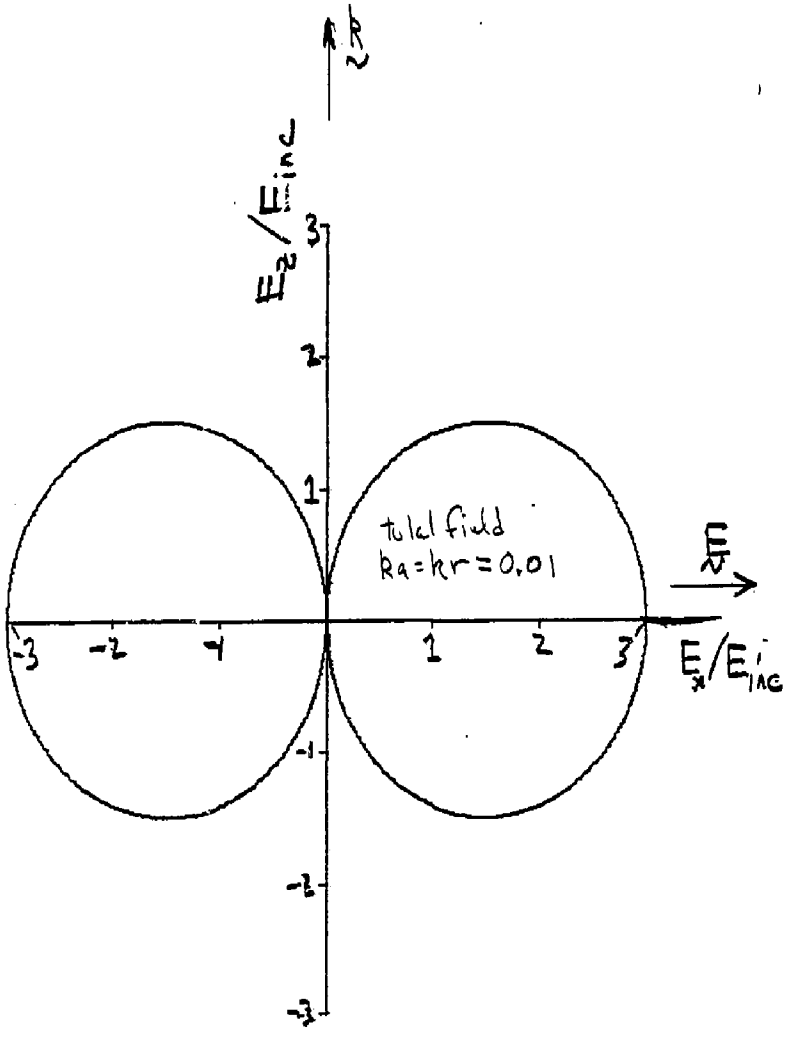
$\hat{z}$
E^z/E^{inc}
3
2
1
-1
-2
-3
-3
-2
-1
1
2
3
total field
$Ka = kr = 0.01$
$\hat{x}$
E_x/E^i_{inc}

Fig. 4.1

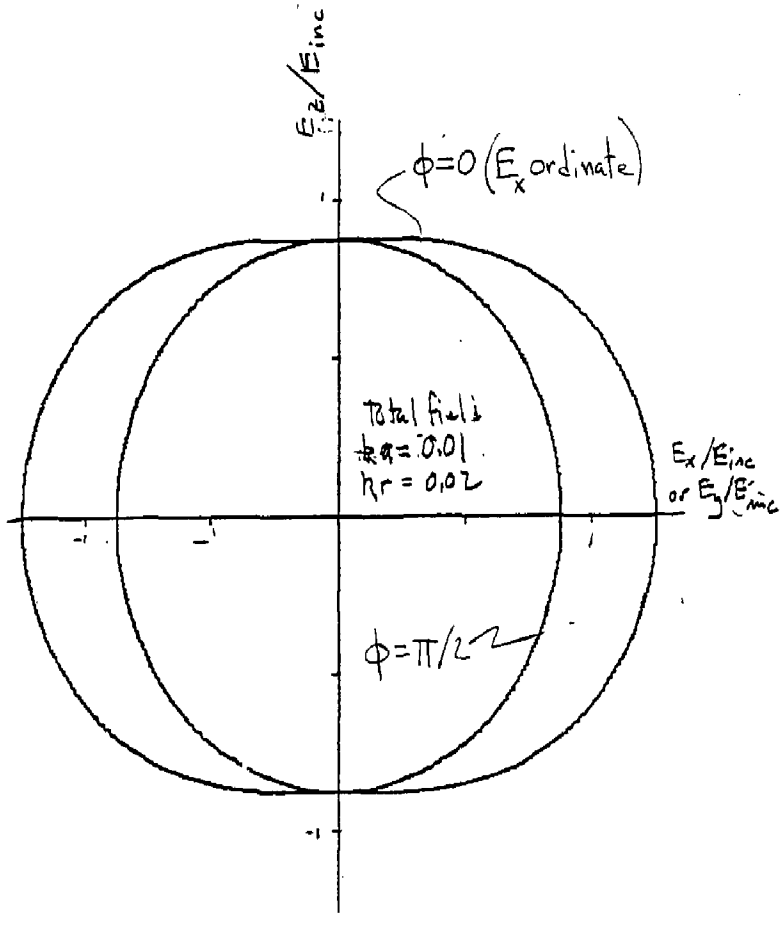
E_z/E_{inc}
$\phi=0$ (E_x ordinate)
Total field
$ka = 0.01$
$kr = 0.02$
E_x/E_{inc}
or E_y/E_{inc}
$\phi=\pi/2$

Fig. 4.2

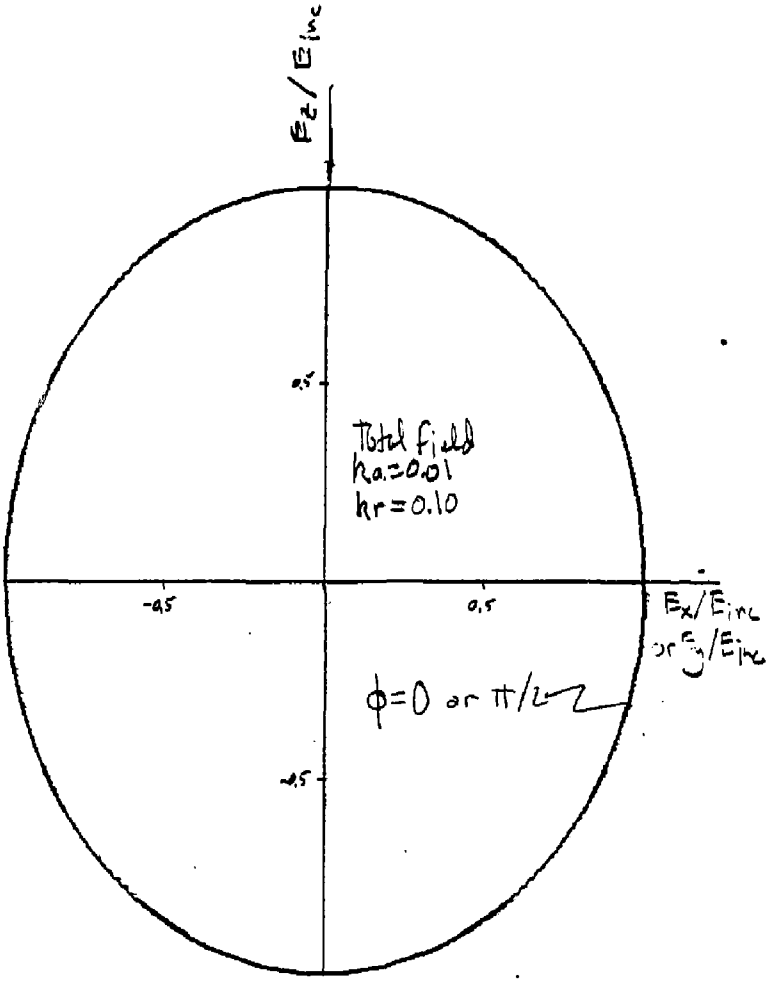
E_z/E_{inc}
0.5
Total field
ka=0.01
kr=0.10
-0.5
0.5
E_x/E_{inc}
or E_y/E_{inc}
$\phi=0$ or $\pi/2$
-0.5

Fig. 4.3

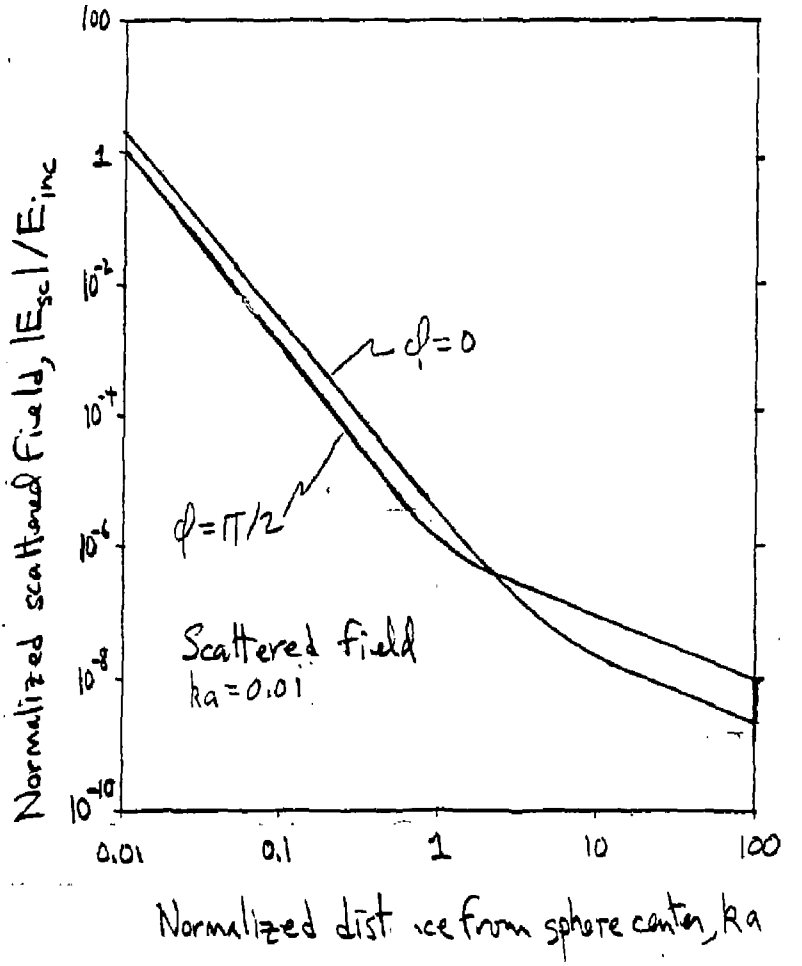
100
1
10^{-2}
10^{-4}
10^{-6}
10^{-8}
10^{-10}
Normalized scattered Field, $|E_{sc}|/E_{inc}$
$\phi = 0$
$\phi = \pi/2$
Scattered field
ka = 0.01
0.01
0.1
1
10
100
Normalized distance from sphere center, ka

Fig. 4.4

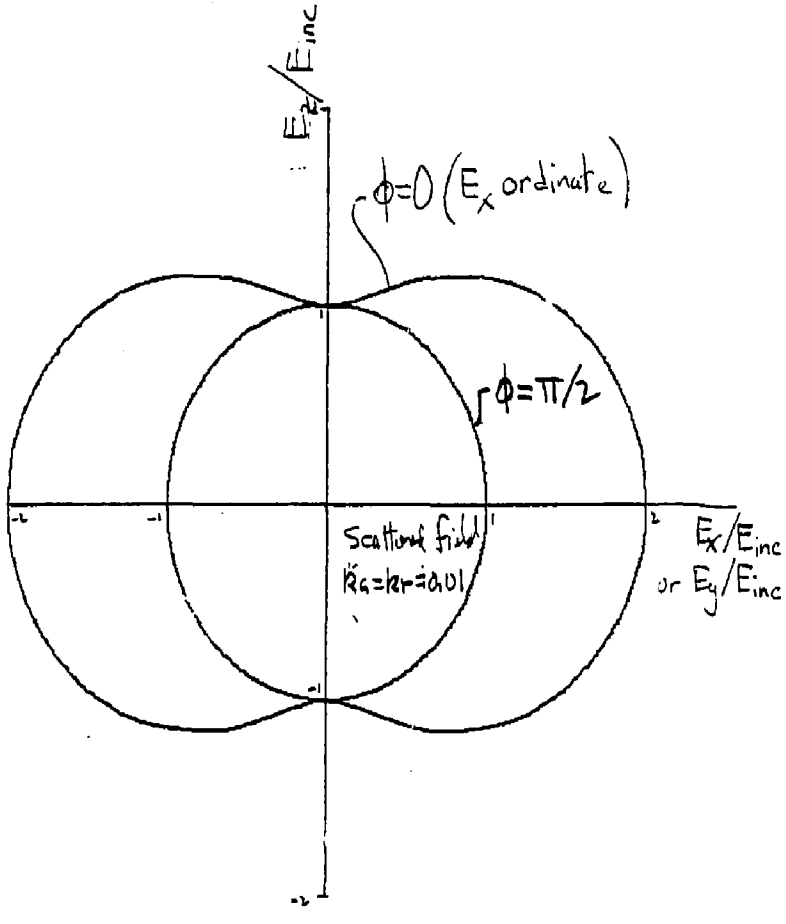
E_z/E_{inc}
$\phi=0$ (E_x ordinate)
$\phi=\pi/2$
Scattered field
$Ka=ka=0.01$
E_x/E_{inc}
or E_y/E_{inc}

Fig. 4.5

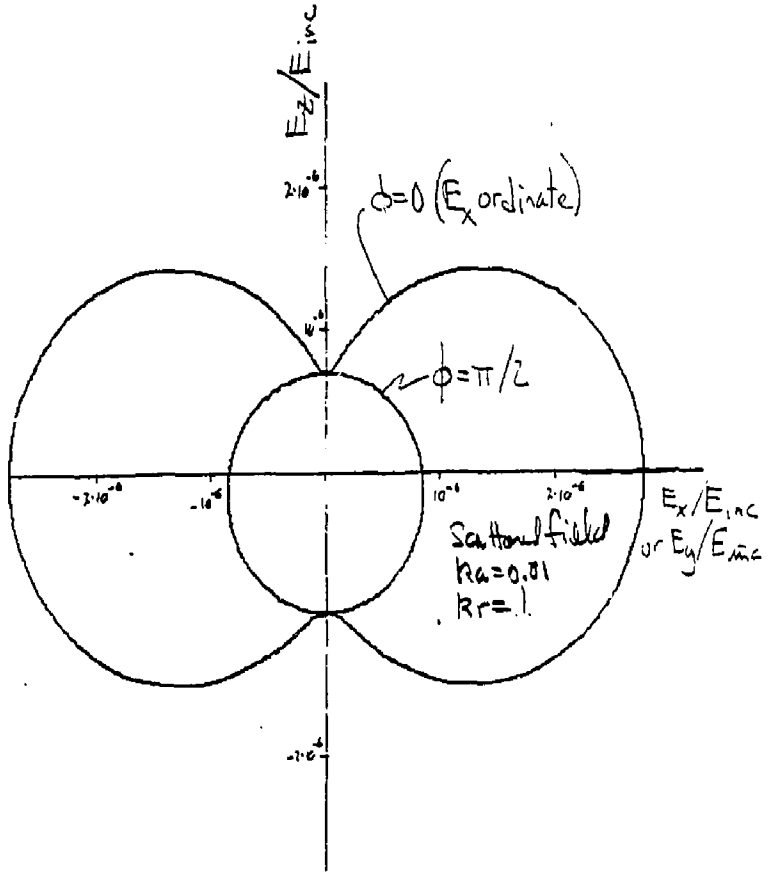
E_z/E_{inc}
$\phi=0$ (E_x ordinate)
$\phi=\pi/2$
E_x/E_{inc}
or E_y/E_{inc}
Scattered field
Ka=0.01
Kr=1

Fig. 4.6

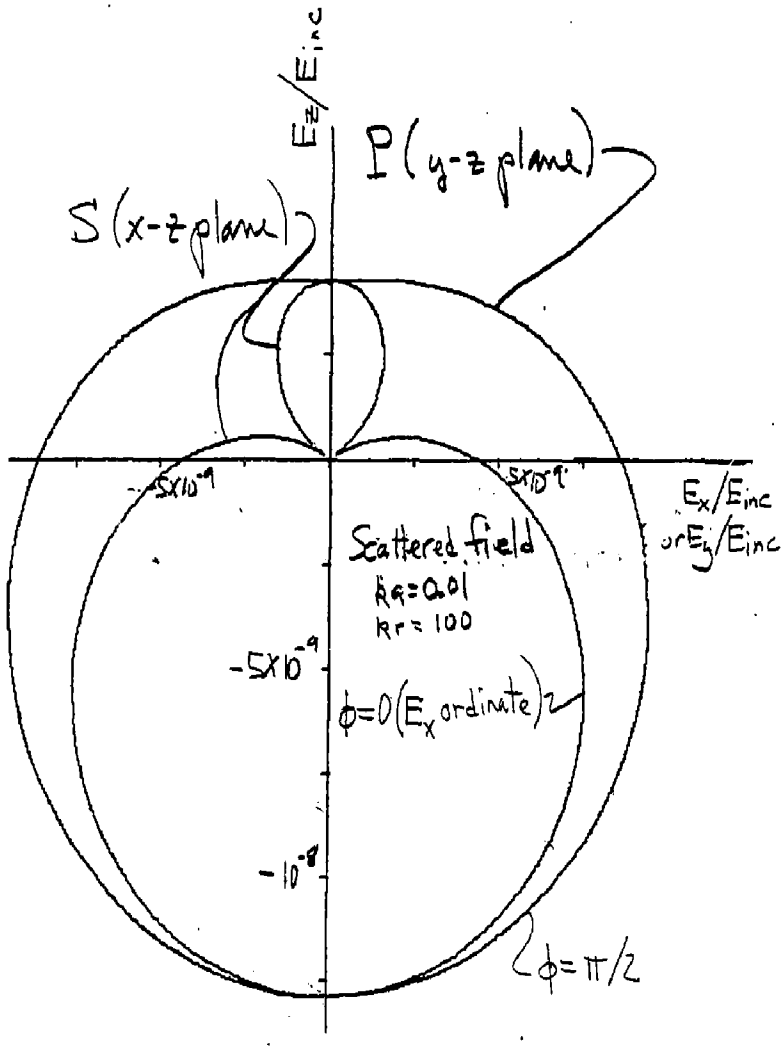
E^{sc}/E^{inc}
P (y-z plane)
S (x-z plane)
5×10^{-9}
-5×10^{-9}
E_x/E_{inc}
or E_y/E_{inc}
Scattered field
ka=0.01
kr=100
-5×10^{-9}
$\phi=0$ (E_x ordinate)
-10^{-8}
$\phi=\pi/2$

Fig. 4.7

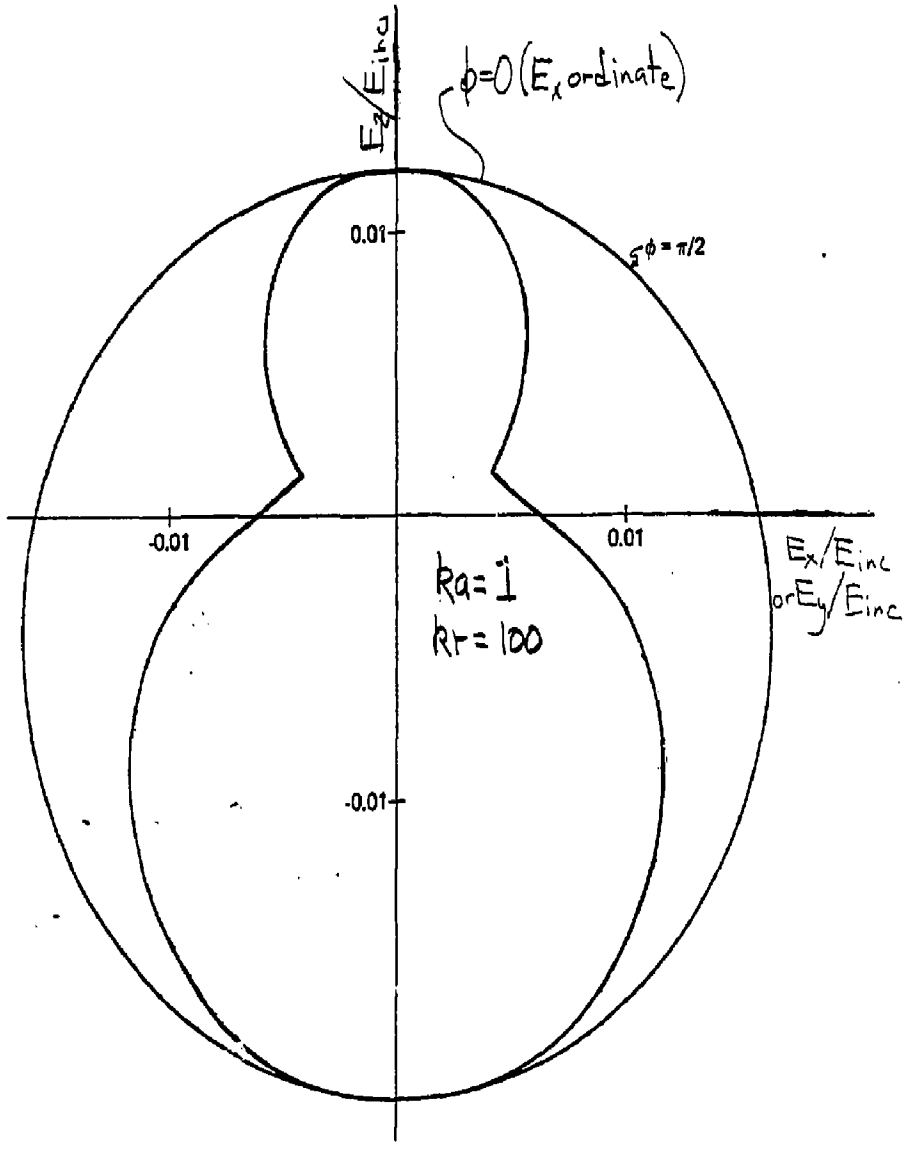
E_z/E_{inc}
$\phi=0$ (E_x ordinate)
$\phi=\pi/2$
0.01
-0.01
-0.01
0.01
E_x/E_{inc}
or E_y/E_{inc}
ka=1
kr=100

Fig. 4.8